An Innovative Tooth Root Profile for Spur Gears and its Effect on Service Life

Ting Zou · Mathew Shaker · Jorge Angeles · Alexei Morozov

Abstract An innovative approach to the design of the gear-tooth root-profile, and its effects on the service life is reported in this paper. In comparison with the widely used trochoidal and the recently proposed circular-filleted root profiles, the optimum profile proposed here is a G^2-continuous curve that blends smoothly with both the involute of the tooth profile and the dedendum circle. Following the AGMA and ISO standards for fatigue loading, the von Mises stress at the critical section and stress distribution along the gear tooth root are studied. The process leading to gear-tooth failure is composed of the crack initiation phase, in number of cycles N_i, and the crack propagation phase, in N_p cycles. The strain-life (ϵ-N) method is employed to determine N_i, where the crack is assumed to initiate at the critical section. Based on the ANSYS crack-analysis module, the effects of G^2-continuous blending on the stress intensity factor (SIF) are investigated for different crack sizes. Paris' law, within the framework of Linear Elastic Fracture Mechanics, is used to correlate the SIF with crack size and, further, to determine N_p. The optimum profile provides a significant reduction in SIF and improvement in both N_i and N_p. Spur gears are made of high-strength steel alloy 42CrMo4, the effects of its properties and surface treatment on service life improvement not being included in this study.

Keywords tooth root-profile optimization · crack initiation · crack propagation · linear elastic fracture mechanics · finite element method

1 Introduction

With the increasing demands on gear transmissions in the automotive and the aerospace industry, spur gears have become the focus of intensive research during the last two decades. As a key component, the reliability of spur gears plays a significant role in the performance of the overall gear transmission system. Reliability depends on two items: 1) the load-carrying capacity of the gear tooth during static or dynamic load transmission via the tooth flanks in contact; and 2) the service life of the gear tooth leading to fatal damage due to fatigue [1]. Each item should not be treated independently; they are interacting. On the one hand, the increase of gear-tooth strength serves as an important factor for the improvement of service life due to fatigue; on the other hand, the critical area for short service life always falls into the stress concentration area, which could contribute to a decrease in the tooth strength.

Generally, gear teeth suffer from three basic types of fracture: impact; fatigue; and "stringers" or "gas pockets" [2]. Fatigue fracture, under consideration in this paper, is caused by an extremely high number of stress cycles on a gear tooth over a certain period. Hence, an optimum gear design with reduced bending stress plays significant roles in improving the fatigue service life. Two approaches are commonly adopted to reduce bending stress for a given tooth size: a) to alter the generating cutter-tooth tip; and b) to modify the gear-tooth root-fillet profile [3]. For the former, different tooth profiles can be generated by assigning different tip radii to the hob. The trochoidal curve, a shape amenable to generation by a hob, is most widely used in the gear industry. According to Buckingham [4], the larger the tip radius of the hob, the lower the bending stress concentration at the gear root. Therefore, compared to its counterpart produced by a rounded-corner hob, the trochoidal root fillet generated by a full-tip-radius hob shows higher bending strength. As explained

Nomenclature

α	crack propagation direction angle	K_I	SIF for fatigue mode I
α_c	pressure angle	K_{Ic}	fracture toughness
β	dimensionless geometric factor	K_{II}	SIF for fatigue mode II
$\Delta\epsilon$	total cyclic strain range	m	material constant
$\Delta\epsilon_e$	elastic strain range	m_t	gear module
$\Delta\epsilon_p$	plastic strain range	n'	cyclic strain-hardening exponent
$\Delta\sigma$	stress range	N_i	crack initiation period
ΔK	stress intensity factor range	N_p	crack propagation period
ϵ'_f	fatigue ductility coefficients	N_t	number of teeth
ν	Poisson ratio	r_a	radius of the addendum circle
σ	uniform tensile stress in a direction normal to the plane of crack	r_b	radius of the base circle
		r_d	radius of the dedendum circle
σ'_f	fatigue strength	r_p	radius of the pitch circle
σ_m	mean stress	s_{Fn}	tooth thickness at the critical point
ξ_F	angle between the fillet tangent and the tooth centerline	APDL	ANSYS Parametric Design Language
		CAE	Computer-Aided-Engineering
a	crack length	DOF	degrees of freedom
a_c	critical crack size	DTA	Damage Tolerance Analysis
a_i	initial crack size	FEM	Finite Element Method
b	strength exponent	HPSTC	Highest Point of Single Tooth Contact
C	material constant	LEFM	Linear Elastic Fracture Mechanics
c	fatigue ductility exponent	MTS	Maximum Tangential Stress
E	Young modulus	OCS	optimum cubic-spline
h_{Fe}	bending moment arm application at the tip	ODA	Orthogonal Decomposition Algorithm
K	stress intensity factor	SIF	stress intensity factor
K'	hardening coefficient		

by Zhao [5], a novel approach was developed to optimize the gear-tooth root profile by optimizing the cutter tip using a rational quadratic Bezier curve. Extensive investigations were conducted on root-fillet profile optimization. Spitas et al. [6] proposed a novel circular fillet design for spur gears instead of the conventional trochoidal fillet. The circular-fillet was proved to be capable of increasing gear-fatigue life via boundary-element analysis. Similar analysis on the comparison between trochoidal and circular fillets was reported by Sankar et al. [7,8,9]. Other types of root-fillet profiles were also analyzed, for instance, the elliptical fillet [10], the optimum fillet produced by polynomial curve fitting [11], as well as that formed by FEA, and a random search method [3].

Fatigue analysis is critical in gear design [12]. The process leading to structural failure is composed of a fatigue crack initiation and a crack propagation phases. The former represents the early stage of fatigue damage, which depends on the micro- and macro-geometry of the specimen, microstructure of the material and the applied load [13]. The prediction of crack initiation is based on the strain-life method, correlating the number of cycles N_i to initiate a fatigue crack with deformation ϵ, and stress σ. This method assumes that the crack is always initiated at the critical location, where the maximum von Mises stress occurs. In the strain-life method, the macroscopic elasto-plastic relations are explained and the plastic effects are described by the local strain range instead of stress range at the critical location [14]. By means of the Ramberg-Osgood description, the local strain range and loading cycles are correlated, considering the cyclic softening and hardening of the material [15]. The total cyclic strain range $\Delta\epsilon$ is composed of the elastic and plastic strain ranges, i.e., $\Delta\epsilon_e$ and $\Delta\epsilon_p$, as

$$\frac{\Delta\epsilon}{2} = \frac{\Delta\epsilon_e}{2} + \frac{\Delta\epsilon_p}{2} = \frac{\Delta\sigma}{2E} + \left(\frac{\Delta\sigma}{2K'}\right)^{1/n'} \tag{1}$$

where E is the Young modulus, K' the hardening coefficient, $\Delta\sigma$ the stress range and n' the cyclic strain-

hardening exponent. Parameters E, K' and n' are material properties, obtained experimentally.

Based on the Ramberg-Osgood relationship recalled in Eq. 1, the strain range at the critical location is correlated with the number of fatigue loading cycles N_i in terms of the Coffin-Manson relation [16,17,18], namely,

$$\frac{\Delta\epsilon}{2} = \frac{\Delta\epsilon_e}{2} + \frac{\Delta\epsilon_p}{2} = \frac{\sigma'_f - \sigma_m}{E}\left(2N_i\right)^b + \epsilon'_f\left(2N_i\right)^c \quad (2)$$

where σ'_f, σ_m and ϵ'_f are the fatigue strength, mean stress and fatigue ductility coefficients, respectively, while b and c are the strength exponent and fatigue ductility exponent, measured from fully tension-compression fatigue tests.

The crack enters the stage of crack propagation once the number of loading cycles is beyond N_i. The Paris law, within the framework of the theory of Linear Elastic Fracture Mechanics (LEFM), relates the stress intensity factor range to the fatigue crack growth, under the fatigue stress [12]. The Paris law is applicable to the prediction of crack growth based upon the assumption that the stress intensity factor (SIF) range ΔK is a function of the crack growth rate, $\mathrm{d}a/\mathrm{d}N_p$, namely,

$$\frac{\mathrm{d}a}{\mathrm{d}N_p} = C\Delta K^m(a) \quad (3)$$

where C and m are material constants, a being the crack length, $\Delta K(a)$ the stress-intensity range factor, i.e., the stress intensity factor difference between the maximum and minimum loading, in units of $\mathrm{MPa}\,\mathrm{m}^{1/2}$:

$$\Delta K = K_{\max} - K_{\min} \quad (4)$$

According to the theory of fracture mechanics, the stress intensity factor (SIF) is defined as a function of crack length a [19]:

$$K = \beta\sigma\sqrt{\pi a} \quad (5)$$

where σ is the uniform tensile stress in a direction normal to the plane of crack, β a dimensionless geometric factor. Based on Eq. 5, the SIF follows:

$$\Delta K = \beta\Delta\sigma\sqrt{\pi a} \quad (6)$$

The Paris law is now expressed as[1]

$$\frac{\mathrm{d}a}{\mathrm{d}N} = C\left(\beta\Delta\sigma\sqrt{\pi a}\right)^m \quad (7)$$

---

[1] Although N is an integer, its values lie in the order of 10^6, for which reason it is common practice to treat it as a real number.

The integration of $\mathrm{d}N$, obtained from eq. (7), with respect to the crack propagation loading cycles N_p yields,

$$\int_0^{N_p}\mathrm{d}N = \int_{a_i}^{a_c}\frac{\mathrm{d}a}{C\left(\beta\Delta\sigma\sqrt{\pi a}\right)^m}$$
$$= \frac{1}{C\left(\beta\Delta\sigma\sqrt{\pi}\right)^m}\int_{a_i}^{a_c}a^{-m/2}\mathrm{d}a \quad (8)$$

which leads to

$$N_p = \frac{2(a_c^{1-m/2} - a_i^{1-m/2})}{(2-m)C(\beta\Delta\sigma\sqrt{\pi})^m} \quad (9)$$

Equation (9) shows an explicit relation between the number of loading cycles for the crack to propagate from the initial crack size a_i at the end of the crack initiation phase, to a_c, the critical crack size. The dimensionless geometric factor β depends on the crack size a. Therefore, for given material parameters C and m, the service life from a_i to a_c, i.e., N_p, can be determined by means of certain numerical tools to build the relation of β with the crack length a.

Of all the fatigue studies on gears, research has mainly focused on developing computational models to predict the service life and investigating the effects of diverse types of material on the fatigue crack growth. Crack initiation is strongly influenced by surface defects, e.g., surface roughness and large amount of inclusions [20]. Surface crack may also take place as a result of a high humid working environment and thermal treatment of the material, because of residual stresses accumulated.

This paper focuses on the gear-tooth breakage problem, the authors proposing a novel methodology to optimize the tooth-root profile, for the improvement of gear service life. Instead of investigating effects of material properties and surface treatment on service life, the authors propose the optimization of the gear tooth-root profile. The most popular standards for tooth-root profile design are AGMA and ISO. Following both standards, the critical section is defined, where the potential crack is initiated under fatigue loading. In this paper, effects of the root profile on the reduction of stress, and further, on the fatigue service life, are investigated. The fatigue analysis results of the proposed optimum gear-tooth root profile are compared with the commonly used root profiles. Conclusions regarding the effects of gear tooth-root profile optimization on the improvement of fatigue service life are drawn. It is noteworthy that this paper focuses on the synthesis of the optimum shape, without considering the limitations imposed by current gear-cutting technology. However, technology

maturing and diversifying by the day, like additive manufacturing [21], means to produce economically the fillets we are proposing here should be feasible in the foreseeable future.

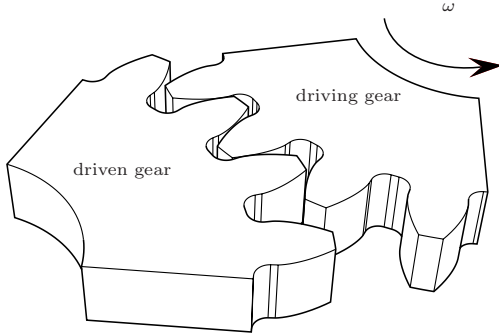## 2 Geometric Modelling of the Spur Gear Tooth

Fig. 1 Spur gears in contact

Figure 1 illustrates the working principle of spur gears under loading conditions. For any tooth, the contact force is applied along the contact line on the flank of the gear tooth, thereby causing a bending stress at the tooth root. Under contact, each gear tooth is assumed to behave as a cantilever beam, subjected to bending. The maximum bending stress of the gear tooth, evolving from the accumulation of normal stress under bending, appears at the root fillet. The gear tooth root is exposed to a combination of both shearing and bending [22]. Due to the maximum stress that the tooth root experiences, the stress intensity and working life of a gear tooth is highly dependent on the tooth-root strength [23]. Moreover, fatigue failure, often taking place at the tooth root [6], occurs in this region due to the repeated stress applied exceeding the yield stress limit of the material; it can thus cause serious defects leading to the breaking of the proper transmission between contacting gears, the whole transmission system thereby failing.

According to the LEFM, crack initiates at the critical section, the one most affected by root stress concentration [24]. For spur gears, both AGMA and ISO standards assume that the maximum stress at tooth root occurs at the critical section. It is noted that the AGMA standard introduces the Lewis-inscribed parabola and defines the critical section as the intersection of the parabola and the tooth root fillet. Figure 2 illustrates the AGMA and ISO standards for the gear tooth-root critical point. In the figure, s_{Fn} is the tooth thickness at the critical point, h_{Fe} the bending moment arm application at the tip, and ξ_F the angle between the fillet tangent and the tooth centerline. As the maximum stress occurs at the critical point F, optimization of the gear tooth-root profile might help to reduce the maximum von Mises stress at that point, thus increasing the crack initiation and crack propagation phases, N_i and N_p. Both standards also define the location of the load applied on the gear tooth. According to both standards, the maximum stress at the tooth root is calculated with respect to the load applied at the Highest Point of Single Tooth Contact (HPSTC) for spur gears.

It is noteworthy that determination of all parameters of the whole gear tooth profile is not available in the AGMA and ISO standards. They provide calculation of the basic important parameters of gear tooth design, namely, s_{Fn}, h_{Fe} and ξ_F, as shown in Fig. 2. For example, according to the AGMA standard, the influence of the number of teeth on design parameters is taken into account. As per Kawalec et al. [22], when the gear is loaded at the HPSTC, the influence of the number of teeth on s_{Fn} and h_{Fe} at the critical point is slight; hence, this influence is neglected in this paper.

Figure 3 illustrates a trochoidal tooth root, commonly used in the design of the gear tooth-root profile [6,25]. The trochoidal root fillet type analyzed herein is produced by the full-tip-radius hob, with a hob radius of 11.33 mm, which leads to lower bending stress concentration compared to its counterpart produced by rounded-corner hob [4]. Besides the trochoidal profile, the circular fillet is also used in the gear industry [3,7]. The circular-filleted profile can be manufactured under a similar cutting process, with a fillet radius of 10.94 mm in this paper, for comparison.

Due to curvature discontinuity at the blending points of the trochoidal and circular fillet with the involute tooth profile and the dedendum circle, stress concentration occurs at those points [26]. Such discontinuities cause a drastic jump in stress values, thereby promoting mechanical failure [27]. A possible approach to reducing fatigue stress at the critical point is the smoothing of the gear tooth-root profile [1].

For the trochoidal, circular and optimum tooth-root profiles, based on both standards, a static, uniformly distributed transmitted load is applied at the HPSTC of the gear tooth. The transmitted load is normal to the tooth flank and pointing to the HPSTC. Both AGMA and ISO standards consider FEM as one of the most accurate methods in determining the gear tooth strength [22]. By means of FEA under ANSYS, the maximum stress is obtained at the critical section of the tooth root.
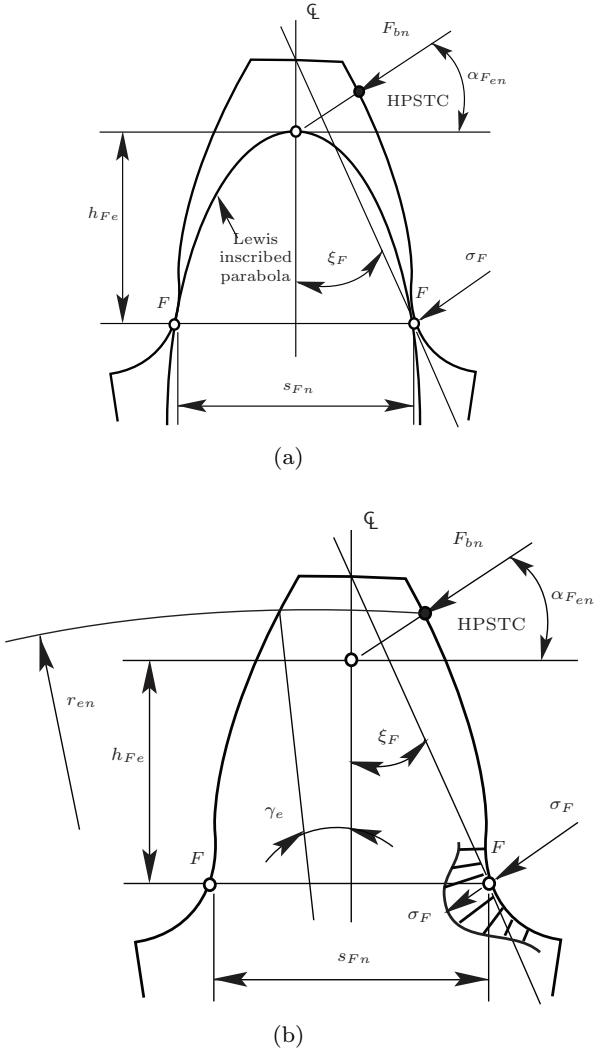
(a)

(b)

Fig. 2 Determination of the critical section, according to (a) AGMA standard 918-A93 and (b) ISO 6336 standard
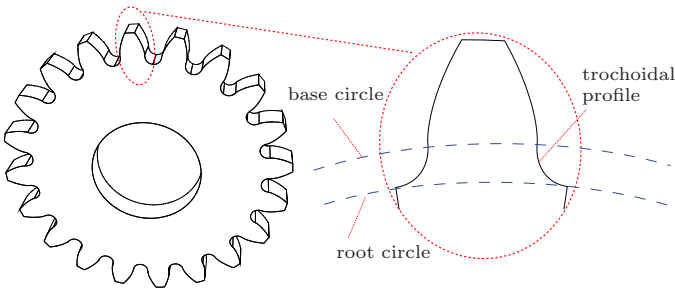

Fig. 3 Gear tooth-root curve shapes

Figure 4 illustrates the 2-D geometry of an involute spur gear tooth, with its dimensions listed in Table 1. The parameter values of the spur gear used in this work were taken from the specialized literature [8]. Spur gears are widely used in high-power planetary transmission (big 2×550 kW excavators). Due to the heavy load
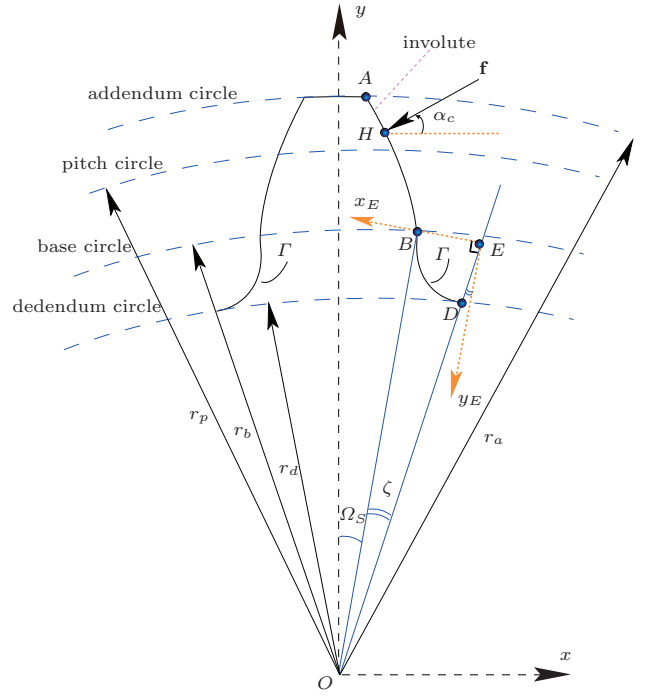

Fig. 4 Geometry of the spur gear tooth [28]

transmitted, spur gears are relatively large. The coordinate frame $\{O, x, y\}$ has its origin at the center of the gear, its y-axis being the axis of symmetry of the gear tooth.

Table 1 Dimensions of the spur gear model

number of teeth N_t	module m_t (mm)	face width (mm)	pressure angle α_C (°)	addendum circle radius r_a (mm)
20	24	350	20	264

pitch circle radius r_p (mm)	base circle radius r_b (mm)	dedendum circle radius r_d (mm)	Ω_S (°)	ζ_m (°)
240	225.5262	210	5.35	3.65

The involute profile is widely used in gear-tooth design, due to its ease of high-precision manufacturing, low transmission error, silent operation, as well as simplicity of assembly—the latter arises from their robustness to errors in the distance between gear centers—in combination with its capability to maintain a uniform angular-velocity ratio [29,30]. The involute segment $\widehat{AB}$, shown in Fig. 4, is defined by

$$\begin{cases} x_{inv} = r_b(\cos t + t \sin t) \\ y_{inv} = r_b(\sin t - t \cos t) \end{cases}, \quad 0 \le t \le \sqrt{\frac{r_a^2}{r_b^2} - 1} \quad (10)$$

where r_d, r_b, r_p denote the radius of the dedendum circle, the base circle and the pitch circle, respectively.

Generally, the fillet curve bears a complex form, which depends on the form of the cutting finish

tools [31]. For practical purposes, the curve segment Γ, which blends with the involute at point B and with the dedendum circle at point D, functions as the gear tooth-root fillet [23]. Γ is commonly produced in gear design as a circular arc [8,7]. The problem with the circular root fillet lies in that it provides only first order geometric continuity, G^1, at the blending points[2] B and D, which gives rise to stress concentration due to curvature discontinuities [32]. Further, the local stress concentration caused by geometric discontinuities may lead to failure of the structure [13]. The widely used trochoidal fillet only provides G^1-continuity at the blending points also [4]. In order to reduce the stress concentration, an important criterion, G^2-continuity at the blending of two given curve segments, should be satisfied. G^2-continuity means position, tangent and curvature continuity over a given geometric curve [33]. Therefore, the problem at hand is formulated as the optimization of the root profile, implemented by an optimum curve Γ, which connects the blending points B and D with G^2-continuity, *as smoothly as possible.*

The position of point D depends on the value of ζ, the angle between OB and the centerline of gear-tooth space, which satisfies $0 < \zeta \leq \zeta_m$, with ζ_m given as [6]

$$\zeta_m = \frac{\pi}{N_t} - \Omega_S \tag{11}$$

where Ω_S is the angle from the centerline of the tooth to OB, defined as

$$\Omega_S = \pi / (2N_t) + \text{inv}(\alpha_c) \tag{12}$$

N_t being the number of teeth and $\text{inv}(x)$ denoting the *involute function* of x, defined as $\text{inv}(x) \equiv \tan(x) - x$.

It is noteworthy that ζ_m is chosen with the purpose of synthesizing a tooth-root profile with the "smallest possible curvature". The term in quotation marks will be precisely defined in the sequel.

The transmitted load $\mathbf{f}$ is normal to the tooth flank and exerted at the HPSTC—Point H in Fig. 4.

3 Methodology

3.1 Curve synthesis

For the purpose of simplifying the curve synthesis procedure, we resort to non-parametric cubic splines to discretize the tooth-root fillet [34]. This spline is a straightforward and simple numerical tool, that lends itself to applications in industrial shaping. Moreover, the proposed cubic spline can be readily integrated with

---

[2] G^1 continuity means point- and tangent-continuity; not curvature-continuity.

Computer-Aided-Engineering (CAE) software. Figure 5 includes a sketch of the blending segments—the involute and part of the dedendum circle—by means of a third one, Γ, between B and D. The coordinate frame $\{E, x_E, y_E\}$ is built with the y_E-axis parallel to $\overline{OB}$ of Fig. 4. Notice that the segments in this figure pertain to a tooth in the lower half of the gear, as opposed to the tooth of Fig. 4, for ease of representation.
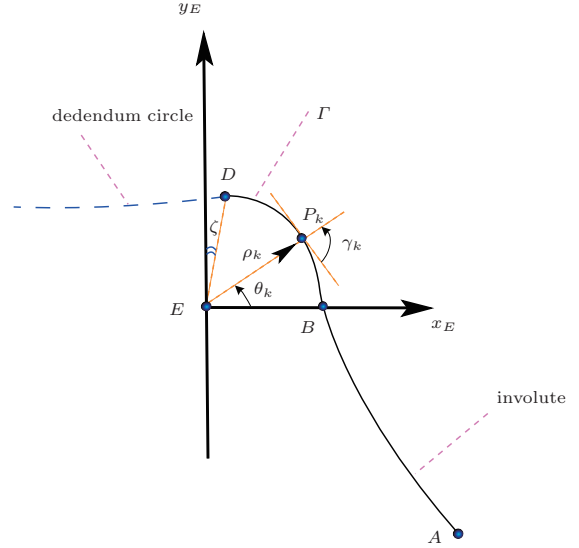

Fig. 5 The blending of the involute and the dedendum circle segment using a G^2-continuous curve fillet, with the same nomenclature of Fig. 4 [28]

Now, $n + 2$ points $\{P_k\}_0^{n+1}$ are defined along the mid-curve segment Γ, by their polar coordinates $P_k(\rho_k, \theta_k)$, with $P_0(\rho_0, \theta_0)$ chosen as B and $P_{n+1}(\rho_{n+1}, \theta_{n+1})$ as D. For point P_k, let $\theta_k = \theta_0 + k\Delta\theta$, for $k = 1, 2, \ldots, n+1$, the *uniform* increment $\Delta\theta$ being

$$\Delta\theta = \frac{\theta_{n+1} - \theta_0}{n+1} \tag{13}$$

Hence, the polar coordinates $\{\rho_k\}_0^{n+1}$ are arrayed in a $(n+2)$-dimensional vector $\boldsymbol{\rho}$, namely,

$$\boldsymbol{\rho} = [\rho_0, \rho_1, \cdots, \rho_{n+1}]^T \tag{14}$$

By the same token, its first- and second-order derivatives $\boldsymbol{\rho}'$ and $\boldsymbol{\rho}''$, are defined with respect to the polar coordinate θ of Fig 5.

According to the definition of non-parametric cubic splines, the cubic polynomial $\rho_k(\theta)$ between two consecutive supporting points P_k and P_{k+1} takes the form [35]

$$\rho_k(\theta) = A_k(\theta - \theta_k)^3 + B_k(\theta - \theta_k)^2 + C_k(\theta - \theta_k) + D_k \tag{15}$$

in which $\theta_k \leq \theta \leq \theta_{k+1}$ and $0 \leq k \leq n$.

By virtue of the G^2-continuity condition, i.e., two curvatures coinciding at the blending point, $\boldsymbol{\rho}$, $\boldsymbol{\rho}'$ and $\boldsymbol{\rho}''$ are found to satisfy the linear relationships below [35]:

$$\mathbf{A}\boldsymbol{\rho}'' = 6\mathbf{C}\boldsymbol{\rho}, \quad \mathbf{P}\boldsymbol{\rho}' = \mathbf{Q}\boldsymbol{\rho} \tag{16}$$

with matrices $\mathbf{A}$, $\mathbf{C}$, $\mathbf{P}$ and $\mathbf{Q}$ provided in the Appendix.

Further, the curvature at P_k takes the form, in polar coordinates,

$$\kappa_k = \frac{\rho_k^2 + 2(\rho_k')^2 - \rho_k\rho_k''}{[\rho_k^2 + (\rho_k')^2]^{3/2}} \tag{17}$$

Now, if a curve with "the smallest possible curvature" is sought, an obvious candidate is a curve Γ with a curvature distribution that carries the minimum root-mean-square value in the segment comprised between B and D of Fig. 4. Hence, the optimization problem is formulated as

$$z = \frac{1}{n} \sum_{k=1}^{n} w_k \kappa_k^2 \longrightarrow \min_{\mathbf{x}}, \quad \mathbf{x} = [\rho_1 \quad \cdots \quad \rho_n]^T$$

subject to

$$\begin{aligned} \kappa_0(\boldsymbol{\rho}, \boldsymbol{\rho}', \boldsymbol{\rho}'') &= \kappa_B = 1/r_b, \\ \kappa_{n+1}(\boldsymbol{\rho}, \boldsymbol{\rho}', \boldsymbol{\rho}'') &= \kappa_D = 1/r_d \end{aligned} \tag{18}$$

in which w_k denotes a *normalized weight* at point P_k, obeying $\sum_{k=1}^{n} w_k = 1$. Besides, with reference to Fig. 4, the additional boundary constraints at the two blending points are

$$\begin{cases} \theta_0 = \theta_B = 0 \\ \theta_{n+1} = \theta_D = \dfrac{\pi}{2} - \zeta_m \end{cases}, \quad \begin{cases} \rho_0 = \rho_B = r_b \tan \zeta_m \\ \rho_{n+1} = \rho_D = \dfrac{r_b}{\cos \zeta_m} - r_d \end{cases} \tag{19}$$

The optimization problem thus formulated is a constrained nonlinear mathematical program, which can be solved using a suite of methods, the one used here is the in-house developed ODA (orthogonal decomposition algorithm) [36].

3.2 Co-simulation

Upon the geometry synthesis of the root profile, the optimization problem formulated in Sec. 3.1 is implemented via co-simulation by means of the ODA package implemented in Matlab and the FEA using a customized ANSYS Parametric Design Language (APDL).

The procedure starts with equal weights for all supporting points, i.e., $w_k = 1/n$, the coordinates for all supporting points being generated to form the initial cubic-splined tooth profile. The optimum found with equal weights is termed the *geometric optimum*. Based on the G^2-continuity constraints, the geometric optimum is capable of reducing the stress concentration to some extent. However, there is still room for improvement. Hence, a set of iterations is conducted, to find the root profile with minimum von Mises stress distribution.

Based on the generated point coordinates and the geometric parameters from Matlab, the gear tooth is modeled in ANSYS and meshed consecutively. Then, a static analysis is conducted by applying the boundary conditions and loadings, which produces the von Mises stress at each supporting point along the root-fillet profile. Aiming to alleviate the stress concentration along the splined fillet, different weights in eq. (18) are assigned to each supporting point according to their corresponding von Mises stress values s_k, as reported by ANSYS:

$$w_k = s_k / \sum_{i=1}^{n} s_i \tag{20}$$

The idea is that the points with higher von Mises stress values are more heavily penalized by assigning to them a higher weight at the current iteration. The procedure stops when the von Mises stress value remains virtually constant throughout Γ, which yields, in turn, the *most uniform stress distribution*, thereby satisfying Venkayya's optimality criterion[3] [37]. The optimum cubic-splined tooth-root profile is illustrated in Fig. 6. From this figure, it is noteworthy that the optimum fillet is obtained by removing material from its circular counterpart. As illustrated in Fig. 7, the smooth curvature distribution of the optimum profile verifies the structure for a higher allowable bending stress. Hence, the optimum fillet is lighter, yet stronger.

4 Stress analysis

4.1 FE model formulation

Accurate evaluation of the stress at the tooth root and precise determination of the stress distribution require appropriate FE modeling of the tooth. The tooth-root fillet is refined for a more accurate prediction of stress concentration, while the other part of the gear tooth is meshed with relatively larger elements, to lower the computational cost. Figure 8 illustrates the FE model of the gear tooth with its boundary conditions.

---

[3] According to Venkayya's criterion, the optimum design can be interpreted as the one in which the strain energy per unit volume stays constant

Refined mesh at the critical section with 8-node nonlinear quad elements is used for accuracy, while for other areas, larger elements are used for higher computational efficiency. The quad elements at the bottom of the gear tooth show high aspect ratio. However, they are far from the crack propagation path and should not affect the finite element results.

The inherent cyclic symmetry feature of spur gears allows us to take only certain gear segments for analysis; complete FE modeling of the whole spur gear is unnecessarily time-consuming. Some researchers use only one segment of a spur gear for stress analysis [6,38]. As the focus of this study is tooth-root stress minimization, three segments of the spur gear are used to avoid cutting too close to the tooth-root fillet.

The boundary conditions on the generated FE model are defined by fixing all nodes at the inner rim and both radial boundary sections. According to the AGMA standard 918-A93 and ISO standard 6336, the tooth-root stress is calculated with respect to the unit nominal load applied at the HPSTC. Therefore, a unit nominal transmitted load is applied as an external force on the FE model, at its HPSTC, uniformly distributed along the contact line over the tooth width. Instead of evaluating the stress at the tooth root due to the contacts of mating gears, the application of load at the HPSTC to calculate the root stress is also a standard and accurate methodology. By doing this, the complicated contact boundary conditions in FEM are avoided and the development loop procedure is further reduced. The FE model of the gear tooth with both circular and optimum cubic-splined root fillet is used for fatigue stress analysis.

4.2 Shape optimization

Within the framework of previous work [28], using FEA, a set of iterations is conducted to reach the op-
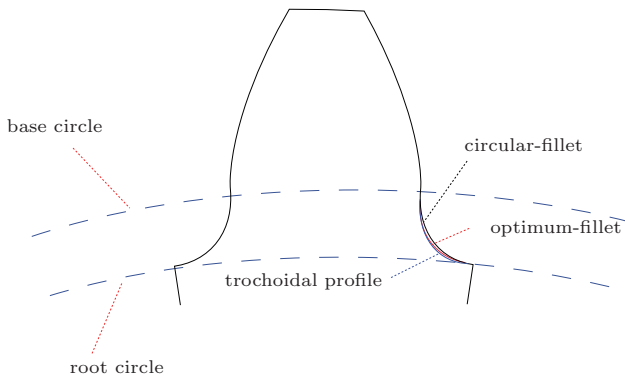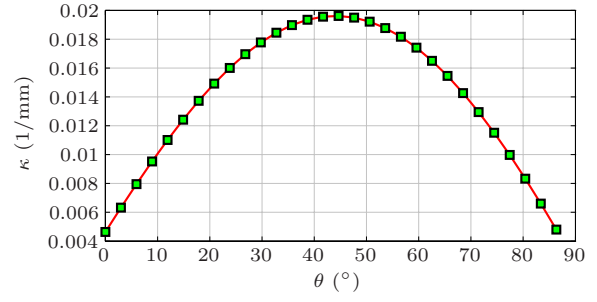

Fig. 7 Curvature distribution over the optimum cubic curve
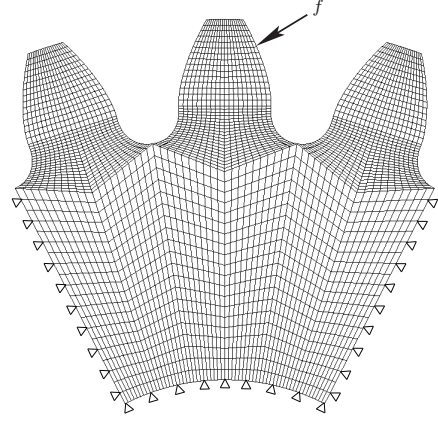

Fig. 8 Finite element mesh for the gear tooth boundary conditions, with 3240 elements and 6862 nodes for the cubic spline model

timum shape profile of the gear tooth-root. The maximum von Mises stress at the gear root versus the number of iterations is illustrated in Fig. 9, from which we can observe that the stress value shows a significant decrement at the first and second iterations, then it starts settling down to the minimum. The optimization procedure stopped at its seventh iteration, when the maximum stress reduction from the previous iteration is smaller than 0.01 MPa. The process was not stopped at the second iteration, when the von Mises stress reaches its minimum value, in the hope that further iterations would lead to an even lower value.

By means of nonlinear analysis in ANSYS, the von Mises stress distribution of the whole gear tooth with the trochoidal, circular and cubic-spline fillets are illustrated in Figs. 10(a), (b) and (c), respectively. It is apparent that the critical von Mises stress occurs within the same region for all profiles, namely, the critical section, which, in this analysis, is within the tensile or loaded side of the tooth. Moreover, the most critical von Mises stress of the cubic-spline is 18% and 14% lower than its trochoidal and circular counterparts, respectively. The FEA results validate the capability of the optimum shape profile in reducing stress concentra-
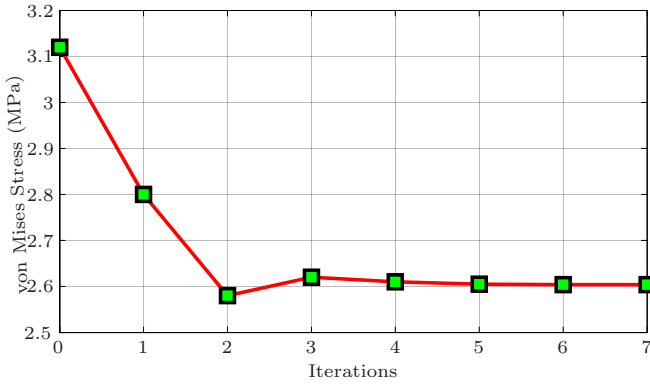

Fig. 6 Gear tooth-root curve shape optimization [28]

Fig. 9 Optimum number of iterations

tions, which plays a significant role in increasing both the crack-initiation and the crack-propagation phases.

5 Fatigue service life improvement

High-strength alloy steel 42CrMo4[4] is used in this work, with Young modulus $E = 2.1 \times 10^5$ MPa and Poisson ratio $\nu = 0.3$ [39].
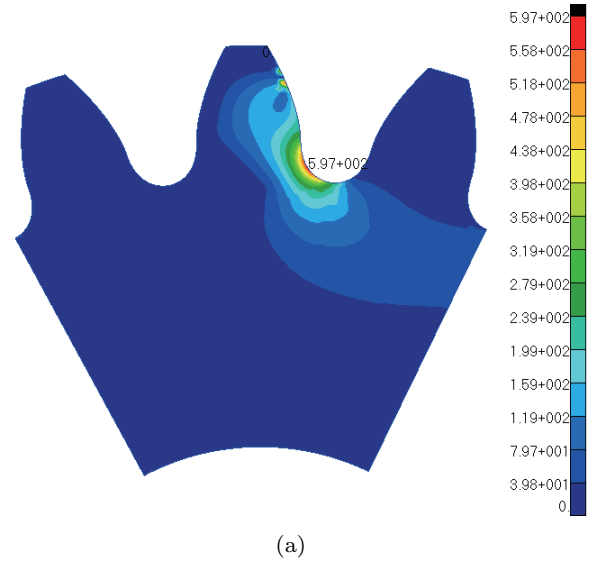
5.1 Fatigue crack initiation

Based upon the von Mises stress from nonlinear FEA, the strain at the critical section is obtained. The fatigue crack initiation phase can be determined by means of the strain-life method, i.e., the ϵ-N_i method. Equation (2), providing the relation of the crack initiation phase N_i with strain, is used to determine N_i at the gear-tooth root critical section in this study. The material parameters are readily available [12], which yields $n' = 0.14$, $\sigma'_f = 1820$ MPa, $\epsilon'_f = 0.65$, $b = -0.08$ and $c = -0.76$.

A set of values of the concentrated bending force F is applied at the HPSTC in ANSYS to calculate the von Mises stress at the critical section. The crack initiation phases, for trochoidal, circular and optimum cubic spline-profiles, are listed in Table 2. It is apparent that, thanks to shape optimization, the smooth stress distribution yields a much higher number of stress cycles for crack initiation.
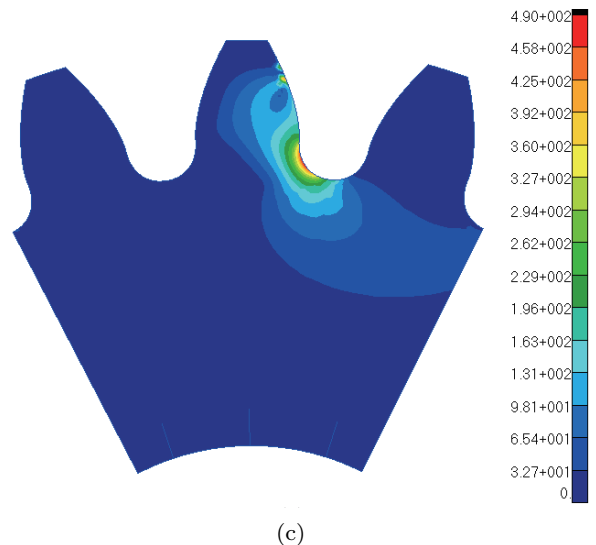
5.2 Fatigue crack propagation

Within LEFM, determination of the crack propagation phase is highly dependent on the SIF at the crack

---

[4] 42CrMo4 contains 0.43% C, 0.22% Si, 0.59% Mn, 1.04% Cr, and 0.17% Mo.
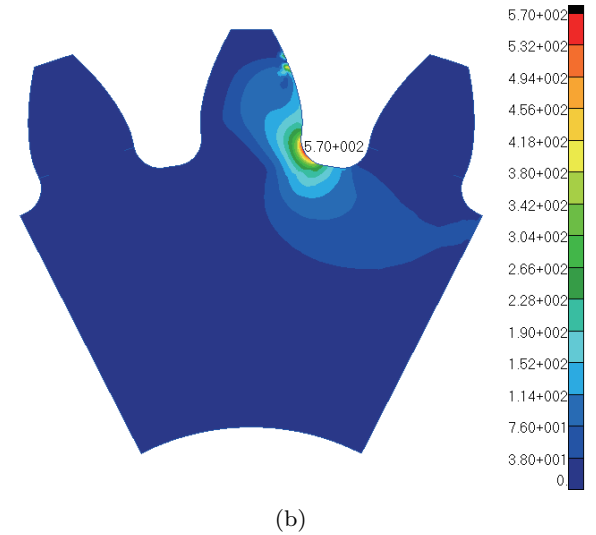
Fig. 10 von Mises stress on (a) the trochoidal profile; (b) the circular-filleted root; (c) the cubic-spline filleted root (MPa)

Table 2 Comparison of fatigue crack initiation phase

Profiles	Load at HPSTC (N)	von Mises Stress (MPa)	N_i (cycles)
trochoidal	1800	597	7.60×10^6
trochoidal	2000	659	2.23×10^6
trochoidal	2200	725	6.62×10^5
trochoidal	2400	786	1.64×10^5
circular	1800	570	1.07×10^7
circular	2000	621	3.46×10^6
circular	2200	685	1.00×10^6
circular	2400	753	2.26×10^5
optimum	1800	490	5.52×10^7
optimum	2000	545	1.12×10^7
optimum	2200	600	8.01×10^6
optimum	2400	660	2.21×10^6

tip [40]. The SIF, according to Eq. (5), is related to the stress and dimensionless geometric factor β at the crack tip. Factor β denotes the variant stress concentration factor corresponding to crack length a and is highly related to the geometry of the mechanical element. Several numerical software tools to calculate β are available, e.g., NASA NASGRO, Bombardier CRPR, etc. However, they only provide β for the basic crack propagation models, e.g., one-tip crack at the edge of a rectangular plate, two-tip crack at the edge of a hole inside a plate, etc. For any complex geometry, determination of the overall β factor is a complicated task, which involves a combination of different basic β factors. By doing this, the approach assumes that any mechanical element profile can be represented by the basic geometries; hence, accuracy is reduced. It is acceptable for commercial engineering projects, where the accuracy requirement is not as strict as in research. However, for the proposed methodology of profile optimization to improve fatigue service life, a more straightforward and accurate approach is preferred.

The FEM, with the aid of a *singular element* at the crack tip to determine the SIF, is used to simulate the crack growth. As illustrated in Fig. 11, a typical singular element forms at least four quadratic elements with 10 nodes around the crack tip. Instead of using specific numerical crack-solving tools, e.g., FRANK2D, the proposed methodology resorts to general FEM software, more readily available. The stress at the crack tip is used to obtain the SIF for fatigue mode I—opening mode with tensile stress normal to the plane of the crack—and II—sliding mode with a shear stress acting parallel to the plane of the crack and perpendicular to the crack front. The SIF for fatigue modes I and II is expressed in terms of normal tensile stress and shear stress, respectively, as [41]

$$K_I = \sigma_n \sqrt{\pi a}, \quad K_{II} = \tau_n \sqrt{\pi a} \tag{21}$$

where σ_n and τ_n are the normal tensile stress and the shear stress at the crack tip, respectively, as illustrated in Fig. 12.
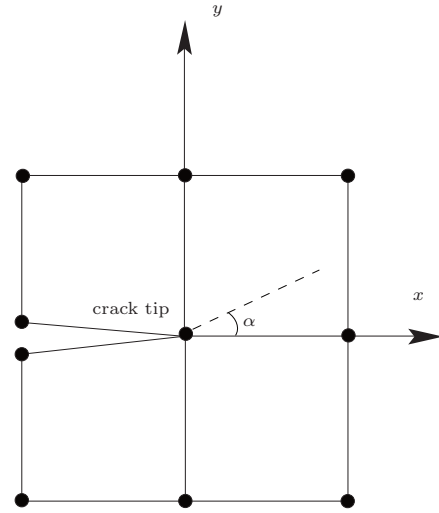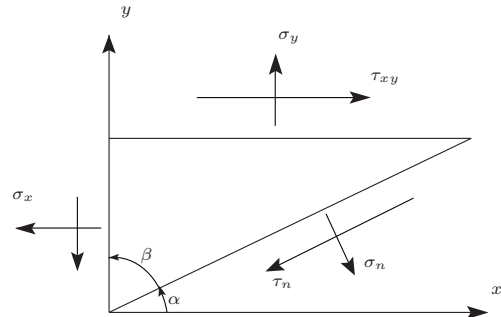
The combined SIF is expressed as

$$K = \sqrt{\left(K_I^2 + K_{II}^2\right)\left(1 - \nu^2\right)} \tag{22}$$

where ν is the Poisson ratio, K_I and K_{II} being the SIF read from ANSYS for fatigue mode I and II, respectively.

According to the Maximum Tangential Stress (MTS) criterion, the crack propagation direction is predicted by angle α, namely,

$$\alpha = 2\arctan\left[\frac{1}{4}\frac{K_I}{K_{II}} + \sqrt{\left(\frac{K_I}{K_{II}}\right)^2 + 8}\right] \tag{23}$$

Fig. 11 FE singular element, with 10 nodes around the crack tip

Fig. 12 Normal tensile stress and shear stress at the crack tip

In the crack propagation simulation, the same loading as in the stage of crack initiation is used. As shown

in Fig. 13, a cyclic loading F is applied at the HPSTC of the gear tooth. One loading cycle corresponds to one contact loading on the HPSTC. The material parameters for crack propagation are taken from [18]: $n = 4.16$ and $C = 3.31 \times 10^{-17}$ mm/cycl/$\left(\text{MPa}\,\text{mm}^{1/2}\right)^{n}$, the fracture toughness being $K_{Ic} = 2620$ MPa mm$^{1/2}$. The initial size of the crack propagation, a_{th}, is set at 1.3 mm in high steel alloys [39]. According to Eq. (3), SIF is a function of crack length a. The critical crack length a_c is reached when the value of SIF is equivalent to the fracture toughness.
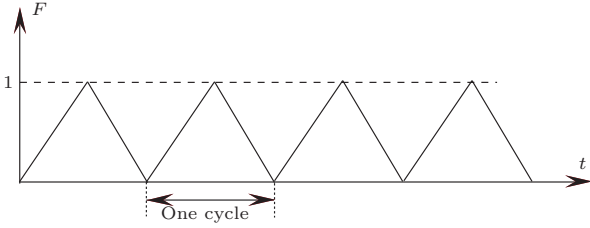

Fig. 13 Loading cycles for FEA crack propagation

With reference to Figs. 10(a), (b) and (c), the crack initiates at the critical section where the highest von Mises stress occurs. The FE model of the crack at the critical section of the tooth root is illustrated in Fig 14. A highly refined mesh is prescribed at the area around the crack tip, for accurate determination of the effects of crack size on the SIF. For different root profiles, a set of simulations is conducted in ANSYS to calculate the SIF for combined fatigue modes, at diverse crack
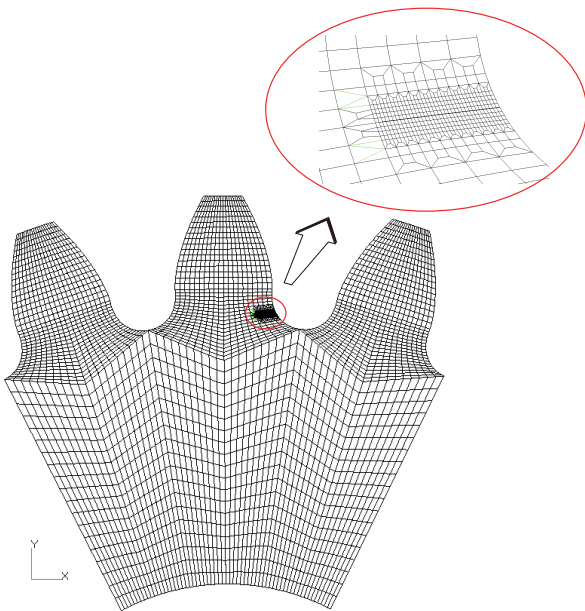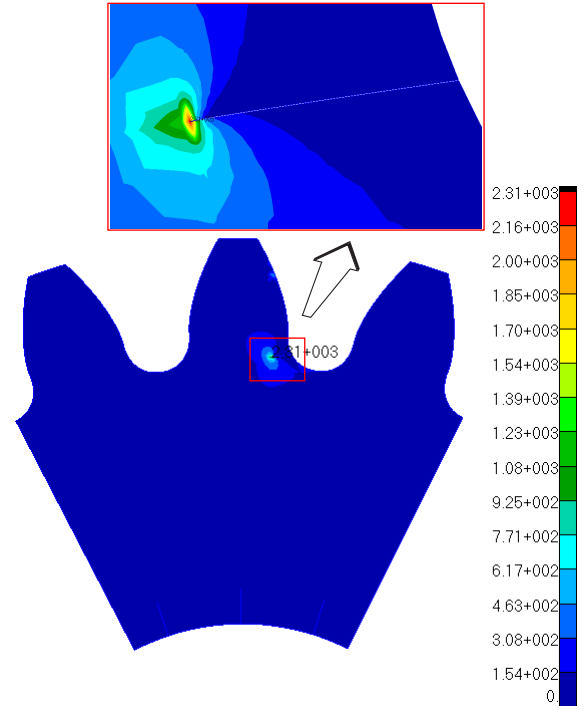

Fig. 15 Stress concentration at the crack tip, in MPa
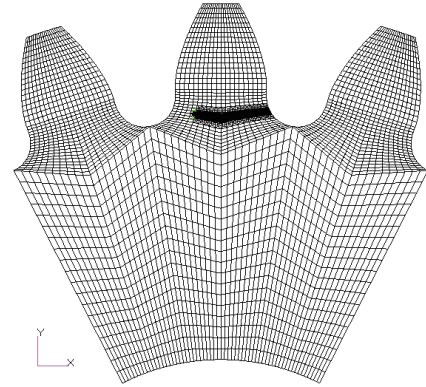
Fig. 16 Predicted crack propagation path
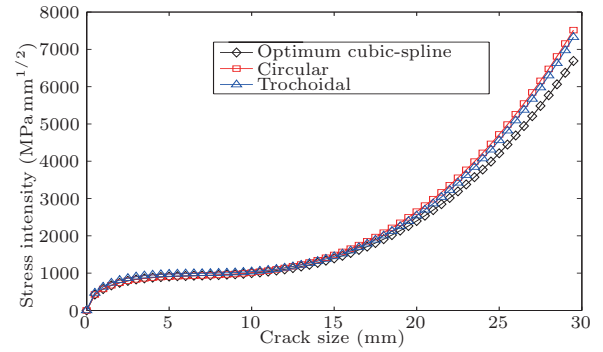
Fig. 17 Crack tip stress intensity factor vs crack size

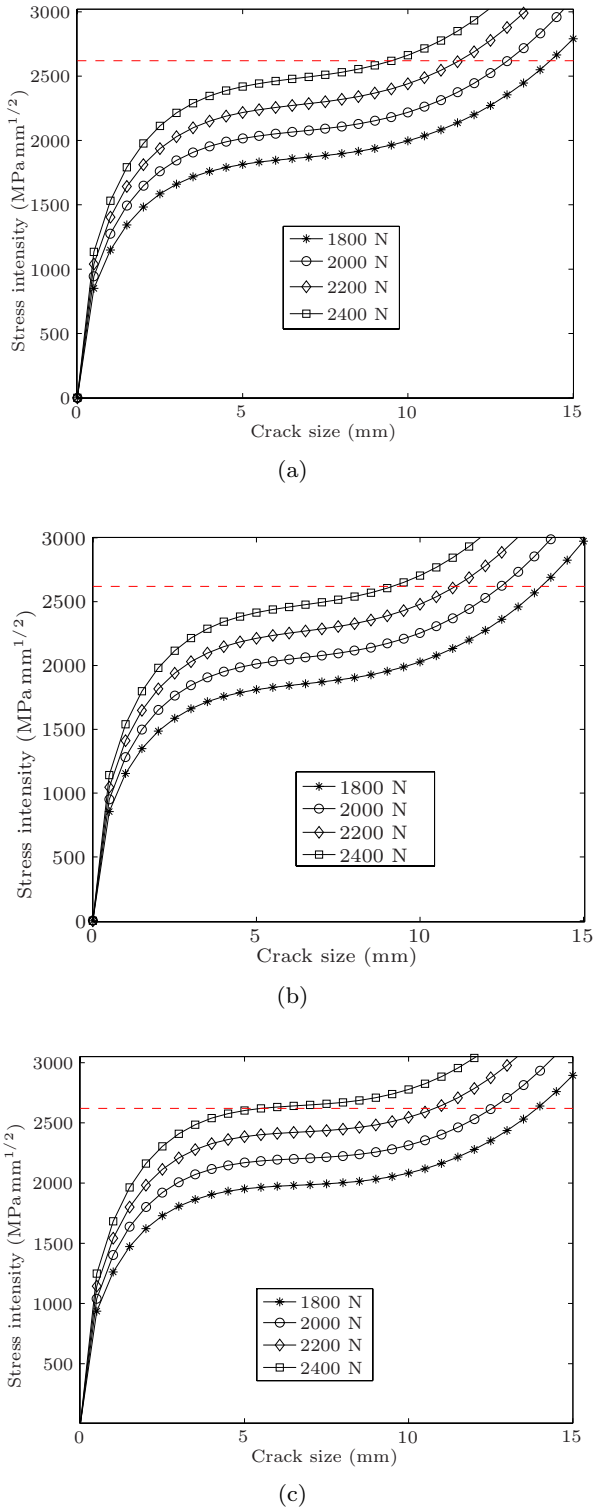**Fig. 14** FE model of the crack tip mesh

(a)

(b)

(c)

Fig. 18 Critical crack length with respect to loadings: (a) optimum cubic-splined fillet (b) circular fillet (c) trochoidal profile
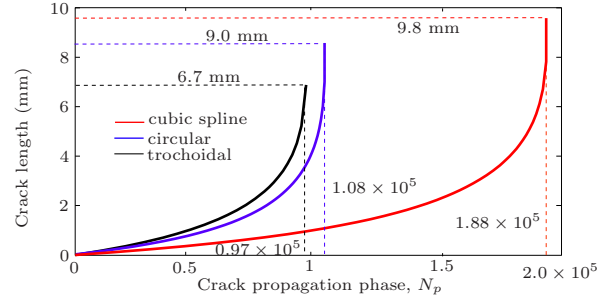

Fig. 19 Crack propagation comparison for different tooth root profiles under 2400 N

lengths. According to Eq. (22), the said SIF is calculated in terms of normal tensile stress and shear stress at the crack tip, as illustrated in Fig. 15. For each simulation, an updated remeshing around the crack tip using a singular element is conducted, until the crack reaches a_c. The crack propagation path is predicted by the crack propagation angle, as per Eq. (23). Figure 16 shows the predicted crack propagation path. As illustrated in Fig. 17, the proposed optimum profile leads to lower stress-concentration levels.

As illustrated in Fig. 18, for trochoidal, circular and optimum cubic-spline root profiles, the critical crack length has a negative relationship with the applied loading. Due to the minimum stress concentration, the critical crack length for the optimum cubic-spline profile is higher than for its trochoidal and circular-filleted counterparts, under the same loading conditions. Higher critical crack lengths help increase the number of cycles N_p for crack propagation, which is obtained using the Paris law. Figure 19 illustrates the crack propagation for the optimum cubic spline, trochoidal and circular-filleted profiles under an applied load of 2400 N at the HPSTC. It is apparent that the proposed optimum root profile leads to a much wider crack propagation phase.

Table 3 lists N_p for different profiles at various applied loads. It is apparent that N_p obeys a negative relationship with load F. Moreover, the effects of profile optimization on the increase of crack propagation cycles are significant. For industrial applications, the crack propagation phase determination is the focus of Damage Tolerance Analysis (DTA), which is significant for in-service engineering in the automotive and the aerospace industry. The increase of crack propagation phase, by means of gear-tooth root profile optimization, is thus feasible.

It is noteworthy that crack initiation accounts for the dominant part of service life. However, with the increase of applied loading, the percentage for which the crack initiation phase accounts through the overall service life decreases.

Table 3 Comparison of fatigue crack propagation phase

Profiles	Load at HPSTC (N)	von Mises Stress (MPa)	N_p (cycles)
trochoidal	1800	597	2.56×10^5
trochoidal	2000	659	1.83×10^5
trochoidal	2200	725	1.32×10^5
trochoidal	2400	786	9.97×10^4
circular	1800	570	2.99×10^5
circular	2000	621	2.23×10^5
circular	2200	685	1.61×10^5
circular	2400	753	1.08×10^5
optimum	1800	490	5.01×10^5
optimum	2000	545	3.49×10^5
optimum	2200	600	2.53×10^5
optimum	2400	660	1.88×10^5

6 Conclusions

The authors proposed an innovative methodology for spur-gear root-profile optimum design, and showed its effects in gear service life. The optimization of the gear tooth-root profile is realized by means of non-parametric cubic splines—parametric cubic splines, ideal for shape optimization, were avoided, because they double the number of design variables, thereby leading to a more complex optimization procedure. The optimum cubic splines provide G^2-continuity at the blending points, while the traditional trochoidal and the recently proposed circular fillet do not. Based on the AGMA and ISO standards, under the same applied loading at the HPSTC, the von Mises stress at the critical section for the general circular-filleted and optimum profiles are obtained by means of ANSYS and compared with each other. The optima led to a significant von Mises stress reduction when compared with their corresponding trochoidal and circular counterpart values. The stress distribution along the gear tooth-root profile was also studied, by recording the von Mises stress value at each node of the FE model on the root profile. The stress distribution of the optimum root profile is the smoothest possible, which led to a significant reduction in stress concentration.

High-strength alloy steel 42CrMo4 is assumed to be the gear material. Investigation of the effects of material properties and surface treatment on service life are beyond the objectives of this study. The overall fatigue phase at the critical section leading to gear-tooth failure is composed of a crack initiation phase N_i and a crack propagation phase N_p. The former accounts for most of the overall service life. Due to both the reduction of the von Mises stress at the critical section and a smooth stress distribution along the tooth-root profile, the proposed optimum profile is advantageous over its trochoidal and circular-filleted counterparts. The determination of crack propagation is realized by Paris law, within the framework of Linear Elastic Fracture Mechanics. Indeed, the proposed fillet increases significantly the number of cycles toward crack initiation and crack propagation.

The proposed methodology provides a straightforward and feasible means in silico, not only for increasing load-carrying capacity, but also for improving service life.

Acknowledgements

Appendix: Matrices Related to the G^2-Continuity Conditions

$$\mathbf{A} = \Delta\theta \begin{bmatrix} 2 & 1 & 0 & 0 & \cdots & 0 & 0 \\ 1 & 4 & 1 & 0 & \cdots & 0 & 0 \\ 0 & 1 & 4 & 1 & \cdots & 0 & 0 \\ \vdots & \vdots & \ddots & \ddots & \ddots & \vdots & \vdots \\ 0 & 0 & \cdots & 1 & 4 & 1 & 0 \\ 0 & 0 & 0 & \cdots & 1 & 4 & 1 \\ 0 & 0 & 0 & \cdots & 0 & 1 & 2 \end{bmatrix} \quad (24)$$

$$\mathbf{C} = \frac{1}{\Delta\theta} \begin{bmatrix} c_{11} & 1 & 0 & 0 & \cdots & 0 & 0 \\ 1 & -2 & 1 & 0 & \cdots & 0 & 0 \\ 0 & 1 & -2 & 1 & \cdots & 0 & 0 \\ \vdots & \vdots & \ddots & \ddots & \ddots & \vdots & \vdots \\ 0 & 0 & \cdots & 1 & -2 & 1 & 0 \\ 0 & 0 & 0 & \cdots & 1 & -2 & 1 \\ 0 & 0 & 0 & \cdots & 0 & 1 & c_{n''n''} \end{bmatrix} \quad (25)$$

in which $n'' = n + 2$, $c_{11} = -1 - \Delta\theta/\tan(\gamma_0)$ and $c_{n''n''} = -1 - \Delta\theta/\tan(\gamma_{n+1})$.

$$\mathbf{P} = \Delta\theta \begin{bmatrix} \frac{1}{\Delta\theta} & 0 & 0 & 0 & \cdots & 0 & 0 \\ 1 & 4 & 1 & 0 & \cdots & 0 & 0 \\ 0 & 1 & 4 & 1 & \cdots & 0 & 0 \\ \vdots & \vdots & \ddots & \ddots & \ddots & \vdots & \vdots \\ 0 & 0 & \cdots & 1 & 4 & 1 & 0 \\ 0 & 0 & 0 & \cdots & 1 & 4 & 1 \\ 0 & 0 & 0 & \cdots & 0 & 0 & \frac{1}{\Delta\theta} \end{bmatrix}$$

$$\mathbf{Q} = \frac{1}{\Delta\theta} \begin{bmatrix} \frac{1}{\tan(\gamma_0)} & 0 & 0 & 0 & \cdots & 0 & 0 \\ -3 & 0 & 3 & 0 & \cdots & 0 & 0 \\ 0 & -3 & 0 & 3 & \cdots & 0 & 0 \\ \vdots & \vdots & \ddots & \ddots & \ddots & \vdots & \vdots \\ 0 & 0 & \cdots & -3 & 0 & 3 & 0 \\ 0 & 0 & 0 & \cdots & -3 & 0 & 3 \\ 0 & 0 & 0 & \cdots & 0 & 0 & \frac{1}{\tan(\gamma_{n+1})} \end{bmatrix}$$

$$(26)$$

References

1. Z. Wang, N. Zhang, D. Dong, and X. Chen, "Analysis of the influence of fillet curves on gear bending strength based on space contact," *Applied Mechanics and Materials*, vol. 155-156, no. 2, pp. 1203–1207, 2012.

2. *Understanding Spur Gear Life TRSM0913.* Service Manual, Eaton Corporation, 2011.

3. A. Kapelevich and Y. Shekhtman, "Tooth fillet profile optimization for gears with symmetric and asymmetric teeth," *Gear Technology*, pp. 73–79, September/October, 2009.

4. E. Buckingham, *Analytical Mechanics of Gears.* Dover Publications, Inc., New York, 1988.

5. X. Zhao, "Increasing bending strength in spur gears using shape optimisation of cutting tool profile," *Australian Journal of Mechanical Engineering*, vol. 12, no. 2, pp. 208–216.

6. V. Spitas, T. Costopoulos, and C. Spitas, "Increasing the strength of standard involute gear teeth with novel circular root fillet design," *American Journal of Applied Sciences*, vol. 2, no. 6, pp. 1058–1064, 2005.

7. S. Sankar, M. S. Raj, and M. Nataraj, "Profile modification for increasing the tooth strength in spur gear using CAD," *Engineering*, pp. 740–749, 2010.

8. D. Ristić, "Numerical model for the critical stress determination in spur gears," *Scientific Technical Review*, vol. LVIX, no. 1, pp. 78–86, 2009.

9. S. A. N. Quadri and D. R. Dolas, "Effect of root radii on stress analysis of involute spur gear under static loading," *International Jounral on Recent Technologies in Mechanical and Electrical Engineering (IJRMEE)*, vol. 2, no. 5, pp. 99–103, 2015.

10. A. A. Sanders, "An experimental investigation of the influence of elliptical root shapes and asymmetric teeth on root stresses and bending fatigue lives," Master's thesis, The Ohio State Univesity, Columbus, OH, 2010.

11. F. T. Pulley, M. W. Kipling, G. A. Matson, D. L. Thurman, and B. W. Avery, "Method for producing and controlling a fillet on a gear," 2000, uS Patent 6,164,880.

12. D. Jelaska and S. Podrug, "Gear tooth root fatigue behavior," *Advanced Engineering*, vol. 2, pp. 187–198, 2007.

13. J. A. Collins, *Failure of Materials in Mechanical Design: Analysis, Prediction, Prevention.* Second Ed. John Wiley & Sons, Inc., New York, 1993.

14. M. R. Gosz, *Finite Element Method: Applications in Solids, Structures, and Heat Transfer.* CRC Press, Taylor & Francis Group, Boca Raton, FL, 2006.

15. E. Nikolaidis, D. M. Ghiocel, and S. Singhal, *Engineering Design Reliability Applications: For the Aerospace, Automotive, and Ship Industries.* CRC Press, 2007.

16. V. Radhakrishnan, "On the bilinearity of the Coffin-Manson low-cycle fatigue relationship," *International Journal of Fatigue*, vol. 14, no. 5, pp. 305–311, 1992.

17. J. Lemaitre and J.-L. Chaboche, *Mechanics of Solid Materials.* Cambridge University Press, 1994.

18. S. Glodez, M. Sraml, and J. Kramberger, "A computational model for determination of service life of gears," *International Journal of Fatigue*, vol. 24, pp. 1013–1020, 2002.

19. A. Blarasin, M. Guagliano, and L. Vergani, "Fatigue crack growth prediction in specimens similar to spur gear teeth," *Fatigue Fract. Engng Mater. Struct*, vol. 20, pp. 1171–1182, 1997.

20. S. Suresh, *Fatigue of Materials, 2nd ed.* Cambridge University Press, 1998.

21. A. Flodin and M. Andersson, "Tooth root optimization of powder metal gears—reducing stress from bending and transient loads." Yokohama, Japan: Powder Metallurgy World Congress and Exhibition (PM 2012), October 14–18, 2012.

22. A. Kawalec, J. Wiktor, and D. Ceglarek, "Comparative analysis of tooth-root strength using ISO and AGMA standards in spur and helical gears with FEM-based verification," *ASME Journal of Mechanical Design*, vol. 128, no. 5, pp. 1141–1158, 2006.

23. J. I. Pedrero, I. I. Vallejo, and M. Pleguezuelos, "Calculation of tooth bending strength and surface durability of high transverse contact ratio spur and helical gear drives," *Journal of Mechanical Design, ASME*, vol. 129, no. 1, pp. 69–74, 2006.

24. P. Fernandes, "Tooth bending fatigue analysis in gears," *Engineering Failure Analysis*, vol. 3, no. 3, pp. 219–225, 1996.

25. S. Senthilvelan and R. Gnanamoorthy, "Effect of gear tooth fillet radius on the performance of injection molded nylon 6/6 gears," *Materials and Design*, vol. 27, no. 8, pp. 632–639, 2006.

26. C. Spitas and V. Spitas, "Four-parametric study of the bending strength of circular fillet versus trochoidal fillet in gear tooth design using BEM," *Mechanics Based Design of Structures and Machines*, vol. 35, no. 2, pp. 163–178, 2007.

27. A. Kapelevich and Y. Shekhtman, "Direct gear design: Bending stress minimization," *Gear Technology*, vol. 20, no. 5, pp. 44–47, 2003.

28. T. Zou, M. Shaker, J. Angeles, and A. Morozov, "Optimization of tooth root profile of spur gears for maximum load-carrying capacity." Buffalo, NY: Paper DETC2014-34568, Proc. ASME 2014 Int. Design Engineering Technical Conferences & Computers and Information in Engineering Conference IDETC/CIE 2014, August 17-20, 2014.

29. F. L. Litvin and A. Fuentes, *Gear Geometry and Applied Theory.* Second Ed. Cambridge University Press, Cambridge, UK, 2004.

30. D. Dudley, *Handbook of Practical Gear Design.* First CRC Reprint, Boca Raton, 2002.

31. S. Radzevich, *Theory of Gearing: Kinematics, Geometry and Synthesis.* Taylor and Francis Group, 2012.

32. H. Neuber, *Theory of Notch Stresses: Principles for Exact Calculation of Strength with Reference to Structural Form and Material.* United States Atomic Energy Commission, Office of Technical Information, Translation Series, 1961.

33. J. Angeles, "Synthesis of plane curves with prescribed geometric properties using periodic splines," *Computer-Aided Design*, vol. 15, no. 3, pp. 147–155, 1983.

34. C. P. Teng, S. Bai, and J. Angeles, "Shape synthesis in mechanical design," *Acta Polytechnica*, vol. 47, no. 6, pp. 56–62, 2008.

35. H. Späth, *One Dimensional Spline Interpolation Algorithms.* A. K. Peters Ltd., Wellesley, MA, 1995.

36. C. P. Teng and J. Angeles, "A Sequential-quadratic-programming algorithm using orthogonal decomposition with Gerschgorin stabilization," *J. Mech. Des.*, vol. 123, no. 4, pp. 501–509, 2001.

37. F. Bidault, C. Teng, and J. Angeles, "Structural optimization of a spherical parallel manupulator using a two-level approach." Pittsburgh, Pennsylvania, US: Proc. of the ASME 2001 Design Engineering Technical Conferences and Computers and Information in Engineering Conference, Paper No. DETC2001/DAC-21030, 2001, pp. 297–305.

38. C. Spitas and V. Spitas, "A fem study of the bending strength of circular fillet gear teeth compared to trochoidal fillets produced with enlarged cutter tip radius," *Mechanics Based Design of Structures and Machines*, vol. 35, no. 1, pp. 59–73, 2007.

39. K. Ananda, R. Ravichandra, and M. Mustaffa, "Spur gear crack propagation path analysis using finite element method." Hong Kong, China: Proceedings of the International Multi Conference of Engineers and Computer Scientists, March 14 -16, 2012.

40. D. Lewicki and R. Ballarini, "Effects of rim thickness on gear crack propagation path," *ASME Journal of Mechanical Design*, vol. 119, pp. 88–95, 1997.

41. H. Tada, P. Paris, and G. Irwin, *Stress Analysis of Cracks Handbook*. Third Ed. Amer Soc Mechanical Engineers, Washington, 2000.